



# Effect of Thermomechanical Treatment on Functional Properties of Biodegradable Fe-30Mn-5Si Shape Memory Alloy

S. PROKOSHKIN, Y. PUSTOV, Y. ZHUKOVA, P. KADIROV, S. DUBINSKIY, V. SHEREMETYEYEV, and M. KARAVAEVA

The structure, martensitic  $\gamma \leftrightarrow \varepsilon$  transformation temperatures, Young's modulus, mechanical properties, and electrochemical behavior of Fe-30Mn-5Si (wt pct) biodegradable shape memory alloy subjected to various thermomechanical treatments (TMT) comprising hot rolling or cold rolling with post-deformation annealing were characterized by optical microscopy, energy-dispersive X-ray spectroscopy, X-ray diffraction, differential scanning calorimetry, tensile testing, open circuit potential, and polarization curves measurements in Hanks' solution, as compared to reference heat treatment. The optimum combination of mechanical properties (low Young's modulus, high tensile strength, and appropriate ductility) for biomechanical compatibility was obtained after TMT with hot rolling at 600 and 800 °C due to the formation of favorable dynamically polygonized and recrystallized structures and decrease in the  $\gamma \leftrightarrow \varepsilon$  transformation starting temperature down to the human body temperature. The TMT did not show a significant effect on the corrosion rate as compared to the appropriate corrosion rate after the reference heat treatment. It is concluded that the TMT with hot rolling at 600 or 800 °C, which provides an optimum combination of the required corrosion rate in the simulation body fluid with high biomechanical compatibility, can be considered a promising treatment of Fe-30Mn-5Si biodegradable alloy for bone implants.

<https://doi.org/10.1007/s11661-021-06217-5>

© The Minerals, Metals & Materials Society and ASM International 2021

## I. INTRODUCTION

ONE of the modern trends in biomedical materials science is the development of a new generation of metallic alloys for traumatology, orthopedics, maxilla-facial surgery, dentistry, cardiovascular surgery, and other applications. These materials should be designed to combine high biocompatibility and appropriate physical and mechanical properties, as well as possess the ability to facilitate healing and tissue regeneration with subsequent natural biodegradation upon completion of the process. The need for such materials is because conventional biomedical alloys (stainless steel, cobalt alloys, titanium, and its alloys, noble alloys) do not biodegrade. Moreover, despite the renowned combination of mechanical and

physical-chemical properties, including various aspects of biocompatibility, these materials may possess some long-term drawbacks that can limit their application such as possible allergic reactions, potentially harmful corrosion, accumulation of wear products in human body tissues, insufficient bioactivity, implant loosening, and fatigue failure.<sup>[1-4]</sup>

As an alternative to conventional implantable metals, biodegradable alloys based on magnesium, iron, and zinc have been widely considered.<sup>[5-14]</sup> Magnesium alloys degrade too fast (typically 1 to 4 months), and the dissolution process is dangerously accompanied by gaseous hydrogen evolution. Moreover, magnesium exhibits poor mechanical properties. In contrast, iron dissolves too slow, but at the same time, it possesses a relatively high Young's modulus. Zinc degradation rate values are between those for Mg and Fe, which can be considered acceptable for biodegradable materials. However, Zn alloys exhibit low strength and ductility.

It is generally assumed that the optimum values of the mechanical properties of biodegradable metallic implant materials should be no less than 300 MPa tensile strength and 15 pct elongation to failure, and the lowest possible Young's modulus to ensure biomechanical compatibility with bone tissue.<sup>[1,2,4,9]</sup> Such a

S. PROKOSHKIN, Y. PUSTOV, Y. ZHUKOVA, P. KADIROV, S. DUBINSKIY, V. SHEREMETYEYEV, and M. KARAVAEVA are with the National University of Science and Technology "MISIS", 4 Leninskiy prospekt, Moscow, Russia, 119049. Contact e-mail: zhukova@isis.ru

Manuscript submitted September 10 2020; accepted February 17, 2021.

Article published online March 16, 2021

combination of properties can be achieved with the promising Fe-Mn-Si alloys with a certain composition range where they can exhibit the reversible  $\gamma$ (FCC)  $\leftrightarrow$   $\varepsilon$ (HCP) martensitic transformation and shape memory effect.<sup>[15–17]</sup>

The required conditions for the pronounced shape memory effect to be achieved are the low volume effect during  $\gamma$ -phase crystal lattice transformation into  $\varepsilon$ -martensite and low stacking fault energy. It has been established that Si addition leads to a significant decrease in the volume effect of the  $\gamma \leftrightarrow \varepsilon$  transformation.<sup>[18]</sup> It has also been shown that the critical driving force for the martensitic transformation increases with the Mn content increase and decreases with that of Si.<sup>[19]</sup> The favorable composition range for the pronounced shape memory effect in polycrystalline Fe-Mn-Si alloys is 28–33 wt pct Mn and 4–6 wt pct Si.<sup>[20,21]</sup> Also, the addition of Si at constant Fe and Mn content leads to strengthening of the alloy.<sup>[18]</sup> Liu et al. first suggested using Fe-Mn-Si shape memory alloys as a biodegradable material.<sup>[22]</sup> In addition to its *in vitro* biocompatibility,<sup>[7]</sup> Fe-Mn-Si alloys have been shown to exhibit appropriate biocompatibility and mechanical integrity with bone tissue *in vivo*.<sup>[23,24]</sup>

Despite the considerable number of studies aimed at improving these alloys' functional parameters, including those of powder-metallurgy and mechanically alloyed materials, with various concentrations of Mn, Si, and other elements,<sup>[13,22–46]</sup> the optimum combination of chemical composition and thermomechanical treatment regimes that can result in the appropriate corrosion rate values combined with the reversible martensitic  $\gamma \leftrightarrow \varepsilon$  transformation starting temperature  $M_s$  being close to the human body temperature has not yet been achieved.

Valuable results were obtained in works<sup>[10,47]</sup> where an effective homogenizing thermal treatment was implemented, and the effect of Mn (23–30 wt pct) and Si (5 wt pct) content on the corrosion and electrochemical behavior and the martensitic transformation temperature range was studied. It was shown that the maximum degradation rate exhibited by the Fe-30Mn-5Si alloy tested in Hanks' solution is 3 times higher than that of Fe-30Mn binary alloys and 6 times higher than for pure Fe,<sup>[47]</sup> and the  $M_s$  temperature of the  $\gamma \rightarrow \varepsilon$  transformation amounts to 60 °C. It was emphasized in<sup>[10,47]</sup> that, in the case of bone implant application, the realization of the forward martensitic transformation temperature being close to human body temperature, which leads to lowering of the Young's modulus due to a pre-martensitic lattice softening, is more crucial than the shape memory itself (moreover, the shape recovery process proceeds at unacceptably high temperatures). Indeed, the Young's modulus of the Fe-30Mn-5Si alloy was 2 times lower than that of pure Fe, indicating better biomechanical compatibility.<sup>[10]</sup> The result obtained reveals the possibility of using this alloy as a biodegradable implant material, on the one hand, and indicates the need to elaborate methods for lowering the  $M_s$  temperature while still preserving high mechanical properties and corrosion rates.

The thermomechanical treatment (TMT) comprising various types and schemes of thermal and deformation conditions is well known to be an effective way to control a metallic material's structure and, consequently, its functional properties. In particular, it is possible to sufficiently increase the mechanical properties, the realization degree, and the stability of shape memory and superelasticity effects in shape memory alloys by varying phase, grain, and subgrain structural features.<sup>[17]</sup> Moreover, the differences in structure and phase states can substantially affect the corrosion and electrochemical behavior of the developed materials, which provides the ability to control the degradation rate.

In this respect, the present work aimed to analyze the effects of different TMT regimes, including hot rolling or cold rolling with post-deformation annealing, on the structure,  $\gamma \leftrightarrow \varepsilon$  transformation temperatures, Young's modulus, mechanical properties, and electrochemical behavior in a simulated biological solution mimicking the mineral composition of human bone tissue (Hanks' solution).

## II. MATERIALS AND METHODS

The experimental Fe-30Mn-5Si (wt pct) alloy, hereinafter Fe-Mn-Si, was obtained by vacuum-arc melting with a non-consumable tungsten electrode with a preliminary getter melting (Ti sponge) to remove residual gases from the furnace chamber. Five-time remelting was carried out to ensure the ingot's homogeneity. The chemical composition and elements' distribution in different ingot parts were controlled by energy-dispersive X-ray spectroscopy (EDX) using a *JSM-6480 LV* scanning electron microscope, taking not less than 10 measurements.

The as-melted ingots were subjected to a reference heat treatment (RHT): isothermal annealing at 900°C for 60 minutes with subsequent water quenching. According to,<sup>[5,40]</sup> the RHT regime results in a homogeneous state of chemical composition and structure and therefore, provides the possibility of uniform lowering of the  $M_s$  temperature and Young's modulus.

The TMT regimes of the Fe-Mn-Si samples are listed in Table I. The choice of TMT regimes was determined by the intention to form a well-developed polygonized dislocation substructure or a fine-grained recrystallized structure of the Fe-Mn-Si alloy. It was supposed that TMT should lead to an improvement in the mechanical properties and the lowering of the  $M_s$  temperature.

Hot rolling of the homogenized samples with  $7 \times 13 \times 70$  mm dimensions was carried out by using a laboratory rolling mill *Duo 210* via 3–4 passes without intermediate heating, with an accumulated true strain  $e = 0.3$  and rapid water cooling after the last pass.

The samples after TMT were ground with P 320 to P 4000 emery paper and subsequently mirror-polished in an *ATM Saphir 520* machine using a 3- $\mu$ m diamond suspension.

The structure study was carried out using a *Ver-samet-2 Union 7452* optical microscope with a

**Table I. TMT Regimes for the Fe-30Mn-5Si Alloy**

Regime Designation	Treatment Details
RHT	Reference Heat Treatment: As-homogenized
HR <sub>600</sub>	Hot rolling ( $e^* = 0.3$ ) at 600 °C
HR <sub>800</sub>	Hot rolling ( $e = 0.3$ ) at 800 °C
CR <sub>500</sub>	Cold rolling ( $e = 0.3$ ) + annealing at 500 °C (30 min)
CR <sub>600</sub>	Cold rolling ( $e = 0.3$ ) + annealing at 600 °C (30 min)

\* $e$  is a true (logarithmic) rolling strain equivalent to a 25 wt pct reduction.

magnification of  $\times 50$  to  $\times 1000$ . To reveal the microstructure, the etchant (70 wt pct HNO<sub>3</sub> solution in ethanol, in 4 wt pct HNO<sub>3</sub>: 96 wt pct ethanol ratio) was applied to the polished samples. The grain size was estimated from at least 5 typical microstructure images.

The X-ray diffraction (XRD) analysis was carried out at room temperature using a *DRON-3* diffractometer with CuK $\alpha$  radiation. XRD profiles were taken in the  $2\theta$  range 38 to 100 deg with 0.1 deg step and 3 seconds exposure. A graphite monochromator was used to reduce the background signal. To remove the polishing-induced deformed surface, the samples were etched (70 wt pct HNO<sub>3</sub> solution in ethanol, in 4 wt pct HNO<sub>3</sub>: 96 wt pct ethanol ratio) prior to the XRD study to dissolve the 0.5 mm-thick layer.

To estimate the characteristic temperatures of the forward and reverse martensitic transformations, differential scanning calorimetry (DSC) with a *Perkin Elmer DSC 4000* calorimeter was carried out with a temperature scanning range from  $-50$  to  $+300$  °C, a heating/cooling rate of 10 °C/min, and a sample mass of about 0.005 g. The forward martensitic transformation starting, peak, and finishing temperatures ( $M_s$ ,  $M_p$ , and  $M_f$ , respectively), as well as those for the reverse transformation ( $A_s$ ,  $A_p$ , and  $A_f$ , respectively), were determined from the exo- or endothermic peaks in the DSC curves. The linear intercept method was used for determining the  $M_s$ ,  $M_f$ ,  $A_s$ , and  $A_f$  temperatures.

Static mechanical tensile testing to failure was carried out using a *MTS MiniBionix 858* machine with an external extensometer with a strain rate of 0.02 s<sup>-1</sup>. The stress-strain curves obtained were used to calculate the Young's modulus  $E$ , yield stress  $\sigma_{0.2}$ , ultimate tensile strength  $\sigma_{UTS}$ , and relative elongation to failure  $\delta$  (average for three samples per regime). The apparent (engineering) Young's modulus was calculated as  $tg\alpha$  where  $\alpha$  is a slope angle of a linear part of the loading branch of the stress-strain curve; the error limit for the Young's modulus values amounts to  $\pm 5$  GPa.

Electrochemical characterization was performed using an open circuit potential (OCP) and polarization curves measurement using an electronic *IPC-Pro* potentiostat with a three-electrode glass cell temperature-controlled by a *TW-2 Elmi* thermostat. The plate-like 10  $\times$  10  $\times$  1 mm samples were used for the tests. The test medium was a Hanks' salt solution<sup>[48]</sup>: 8 g NaCl, 0.4 g KCl, 0.12 g Na<sub>2</sub>HPO<sub>4</sub>·12H<sub>2</sub>O, 0.06 g KH<sub>2</sub>PO<sub>4</sub>, 0.2 g MgSO<sub>4</sub>·7H<sub>2</sub>O, 0.35 g NaHCO<sub>3</sub>, 0.14 g CaCl<sub>2</sub>, water-balanced up to 1 l of the solution, pH 7.4, with the temperature maintained at  $37 \pm 1$  °C. The potential

sweep rate for the polarization curves measurement was set at 0.2 mV/s. The saturated Ag/AgCl<sub>2</sub> electrode was used as a reference electrode, and the platinum one served as an auxiliary electrode. For the corrosion rate estimation, the corrosion current density ( $i_{corr}$ ) was extracted from the polarization curves to determine the corrosion rate ( $C_r$ ) of the alloys, as follows<sup>[49]</sup>:

$$C_r = \frac{i_{corr} 10^4 A_{Me}}{n F d_{Me}} 8,76 \text{ mm/year}, \quad [1]$$

where  $i_{corr}$  is the corrosion current density extracted from the polarization curve, A/cm<sup>2</sup>;  $n$ —is the ionic charge ( $n = 2$  for Fe<sup>2+</sup>),  $F = 26,8$  A·h/g-equivalent—Faraday constant,  $A_{Me}$ —atomic weight of the metal, g;  $d_{Me}$ —metal density, g/cm<sup>3</sup>.

### III. RESULTS AND DISCUSSION

#### A. Chemical Composition and Structure of the Fe-Mn-Si Alloy

The EDX results show that the average composition of the Fe-Mn-Si ingots obtained amounts to  $65.6 \pm 0.2$  wt pct Fe,  $29.4 \pm 0.2$  wt pct Mn and  $5.0 \pm 0.1$  wt pct Si, which adequately corresponds to the required concentration ratio.

Figure 1 shows the optical microscopy images of the Fe-Mn-Si alloy microstructure in the homogenized state (RHT) and after various TMT routes aimed at estimating the effect of TMT on the matrix phase ( $\gamma$ -austenite) grain size and shape. It can be seen that hot rolling at 600 °C (HR<sub>600</sub>, Figure 1(b)) does not cause the grain structure refinement as compared to RHT (Figure 1(a)), with the average grain size about 500  $\mu$ m in both cases. An increase in hot rolling temperature up to 800 °C (HR<sub>800</sub>, Figure 1(c)) leads to a decrease in grain size down to about 100  $\mu$ m, which is the result of partial dynamic and/or static recrystallization. The CR<sub>500</sub> and CR<sub>600</sub> treatments do not induce noticeable variations of the grain size compared to RHT, which indicates that the annealing temperature of 600 °C is not enough for the beginning of static recrystallization.

#### B. XRD Analysis

Figure 2 shows the XRD profiles of the Fe-Mn-Si alloy after various treatments. It can be seen from Figure 2 that the predominant phases after the reference treatment are HCP  $\epsilon$ -martensite and FCC  $\gamma$ -austenite.



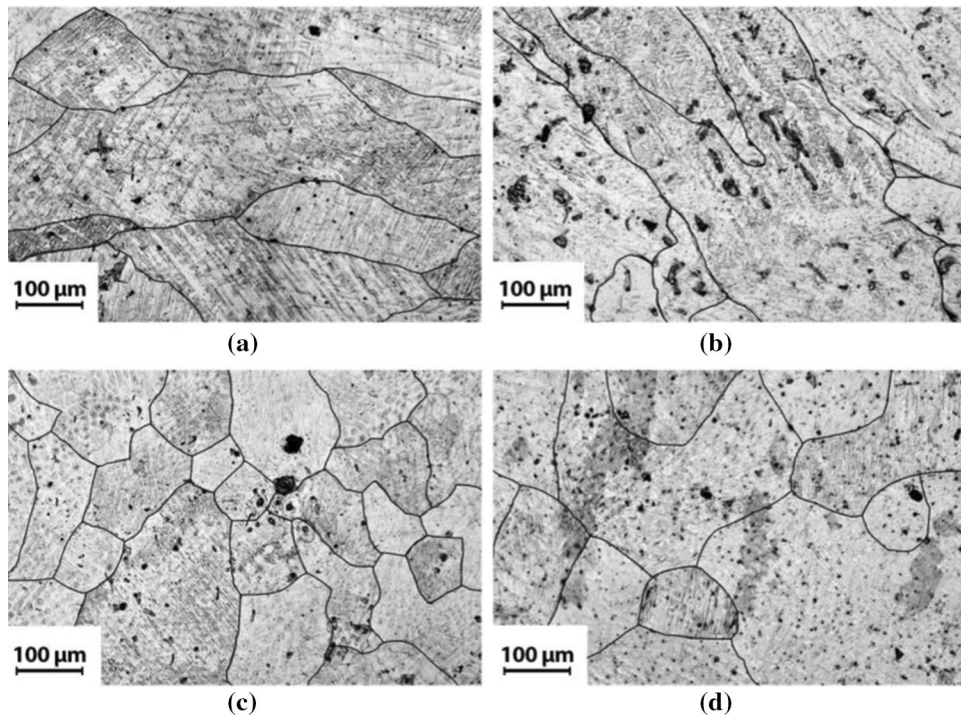


Fig. 1—Light microscopy images of the Fe-30Mn-5Si alloy microstructure after different treatments: (a) RHT, (b) HR<sub>600</sub>, (c) HR<sub>800</sub>, (d) CR<sub>600</sub>. The main grain boundaries are additionally marked with black lines.

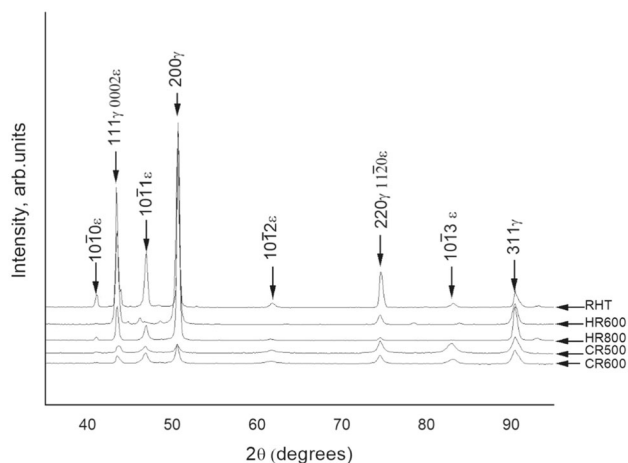


Fig. 2—XRD profiles of the Fe-30Mn-5Si alloy after various treatments.

However, the quantitative analysis of the phase composition is rather complicated due to the overlapping of the main diffraction peaks as well as the influence of the crystallographic texture and large grain size. Visual comparison of the XRD peak intensities shows that all TMT regimes lead to a pronounced decrease in the  $\epsilon$ -martensite content. It can be noted that TMTs using HR and CR regimes cause a significant broadening of the diffraction peaks as compared to the RHT state (Table II). This indicates the formation of the well-developed dislocation substructure as the result of the dynamic recovery and polygonization processes, in the case of HR regimes, and static polygonization, in the

case of CR regimes.<sup>[50,51]</sup> The higher the treatment temperature, the smaller is the broadening of the XRD peaks, evidencing the development of polygonization or possibly recrystallization processes leading to the formation of a less deformed structure (Table II).

### C. DSC Analysis

Figures 3(a) through (c) show typical results of the DSC study of the Fe-Mn-Si alloy after RHT and high-temperature TMTs; Figures 3(d) and (e) give the enlarged fragments of the HR DSC curves to ensure a more precise determination of  $M_s$  and  $M_p$  temperatures, which is of primary practical interest in the context of the treatments' comparison. The data obtained allow for the characteristic temperatures of the reversible martensitic transformations to be measured and the XRD study results to be validated (Section III-B).

It can be seen from Figure 3(a) that the main phase after RHT is  $\epsilon$ -martensite, which corresponds to the results of the XRD analysis. The absence of the  $\epsilon \rightarrow \alpha$  transformation DSC peak can be explained by overlapping with the strong  $\gamma \rightarrow \epsilon$  peak. The RHT state exhibits quite evident calorimetric peaks, while HR treatments show much weaker peaks of the forward and especially reverse transformations, indicating that in these cases they are strongly broadened and incomplete in the studied temperature range. The  $\gamma$ -austenite fraction at room temperature after HR treatments can be evaluated as somewhat below 50 pct because the room temperature is somewhat above  $M_p$  temperatures (Figure 3(b) and (c), Table III). The calorimetric effects of the  $\gamma \leftrightarrow \epsilon$  transformations after CR treatments were too small to

be measured. It should be emphasized again that, from a practical point of view, the characteristic temperatures of the forward transformation are more important for consideration, because decreasing them down to human body temperatures allow the Young's modulus value to be minimized.

Table III summarizes the values of the characteristic temperatures of the forward ( $M_s$ ,  $M_p$ ,  $M_f$ ) and the

reverse ( $A_s$ ,  $A_p$ ,  $A_f$ ) martensitic transformations. It can be seen from Table III that only HR treatment regimes result in a significant decrease in the  $M_s$  temperature, which becomes closer to the required human body temperature of 37 °C. It should be mentioned that the finishing point of the forward  $\gamma \rightarrow \varepsilon$  transformation cannot be found in the DSC curves; therefore, the  $M_f$  temperature can be estimated as below minus 60 °C,

**Table II. The Width of the Diffraction Peaks of the Fe-30Mn-5Si Alloy After Various Treatments (Peak Width at Half-Height,  $2\theta$  Degrees)**

Treatment	$B_{200\gamma}$	$B_{311\gamma}$	$B_{10\bar{1}1\varepsilon}$	$B_{10\bar{1}2\varepsilon}$	$B_{10\bar{1}3\varepsilon}$
RHT	0.35	0.55	0.40	0.66	0.64
HR <sub>600</sub>	0.48	0.76	—	—	—
HR <sub>800</sub>	0.37	0.58	0.51	0.85	—
CR <sub>500</sub>	0.57	0.92	0.63	1.16	1.16
CR <sub>600</sub>	0.55	0.90	0.66	1.50	1.18

**Table III. Characteristic Temperatures of the Forward ( $M$ ) and Reverse ( $A$ ) Martensitic Transformations in Fe-30Mn-5Si Alloy After Various Treatments**

Treatment	$M_s$	$M_p$	$M_f$	$A_s$	$A_p$	$A_f$
RHT	75	58	27	154	182	204
HR <sub>600</sub>	40	8	—	—	—	—
HR <sub>800</sub>	38	14	—	210	243	268
CR <sub>500</sub> *	60	25	—	170	220	—
CR <sub>600</sub> *	70	30	—	130	190	260

\*Approximate temperature values.

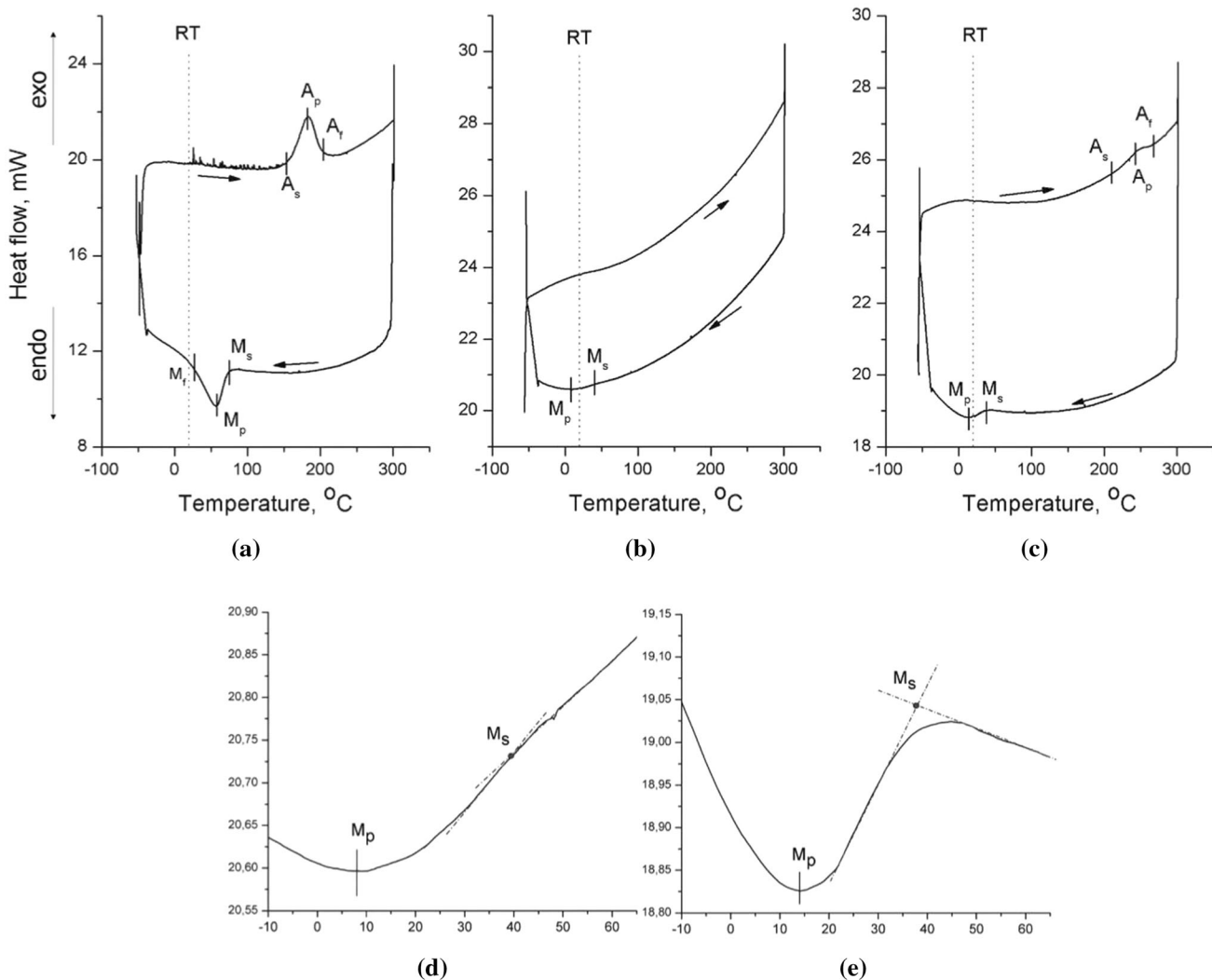


Fig. 3—DSC curves of the Fe-30Mn-5Si alloy: (a) RHT, (b) and (d) HR<sub>600</sub>; (c) and (e) HR<sub>800</sub>; heating/cooling directions are indicated with arrows.

which is the limit of the current experimental setup. The lowering of the  $\gamma \rightarrow \varepsilon$  transformation temperatures after HR treatments can be attributed to the well-known inhibiting effect of the increase in the austenite dislocation density and grain refinement on the martensitic transformation.<sup>[17]</sup>

#### D. Mechanical Testing

Figure 4 shows the stress–strain curves obtained during tensile testing of the Fe-Mn-Si alloy after various treatments. Table IV lists the mechanical parameters derived from the curves obtained: Young’s modulus  $E$ , yield stress  $\sigma_{0.2}$ , relative elongation to failure  $\delta$ , and ultimate tensile strength  $\sigma_{UTS}$ . It can be seen from Table IV that the Young’s modulus of all samples falls in the 80 to 125 GPa range, which is approximately two times lower than that for pure iron (about 220 GPa) and is comparable to pure titanium and its alloys, which have been successfully applied in medicine.

It is important to note that all the TMT preserves a low Young’s modulus value comparable to RHT. It can be explained by pre-transition crystal lattice softening caused by the testing temperature approaching the  $M_s$  temperature.<sup>[17,52,53]</sup> On the one hand, the TMT generally leads to an increase in the concentration of crystal lattice defects (dislocations, subboundaries, and grain boundaries) and results in material stiffening.<sup>[17]</sup> On the other hand, TMT can facilitate the martensitic transformation in shape memory alloys as follows from the Clausius-Clapeyron equation<sup>[54]</sup> and cause the  $M_s$  temperature to decrease<sup>[17]</sup> closer to the deformation temperature, and the Young’s modulus decreases correspondingly. TMT leads to significant strain hardening; therefore, the yield stress is significantly higher for the HR- or CR-treated samples as compared to the

RHT state due to structural and substructural hardening.

The lower  $\sigma_{0.2}$  value for HR<sub>800</sub> compared to the HR<sub>600</sub> regime is related to partial softening during recrystallization, indicating that during hot rolling at 600 °C, the recrystallization process does not yet start. Both regimes ensure quite high values of the elongation to failure, which are comparable to that after RHT (Table IV). In turn, the significant  $\sigma_{0.2}$  increase in the CR regime’s case is caused by the highest lattice defect concentration in the non-recrystallized grains. However, low ductility ( $\delta$ ) restrains the application of these types of TMT regimes. Therefore, it can be concluded that TMT including hot rolling is the advanced treatment procedure for the Fe-Mn-Si alloy compared to cold rolling with post-deformation annealing in terms of high biomechanical compatibility, including a low Young’s modulus, high strength, and sufficient ductility. The relatively low ductility implies the deterioration in functional fatigue properties of the material. The obtained combination of static mechanical properties of the Fe-Mn-Si alloy after HR allows us to expect improvements in the fatigue functional properties of the material. Studies on this topic are in progress.

#### E. Electrochemical Characterization

For biodegradable implantable alloys, the corrosion rate is of principal importance in addition to the structural state. In this regard, electrochemical parameters of the Fe-Mn-Si alloy after various TMT routes were studied in Hanks’ solution and compared to those of pure Armco Fe. Figure 5 shows the OCP curves of the studied materials immersed in Hanks’ solution at 37 °C. It can be seen from the figure that the OCP of all the Fe-Mn-Si alloy samples and Armco Fe shift down towards the negative values, which mainly indicates the

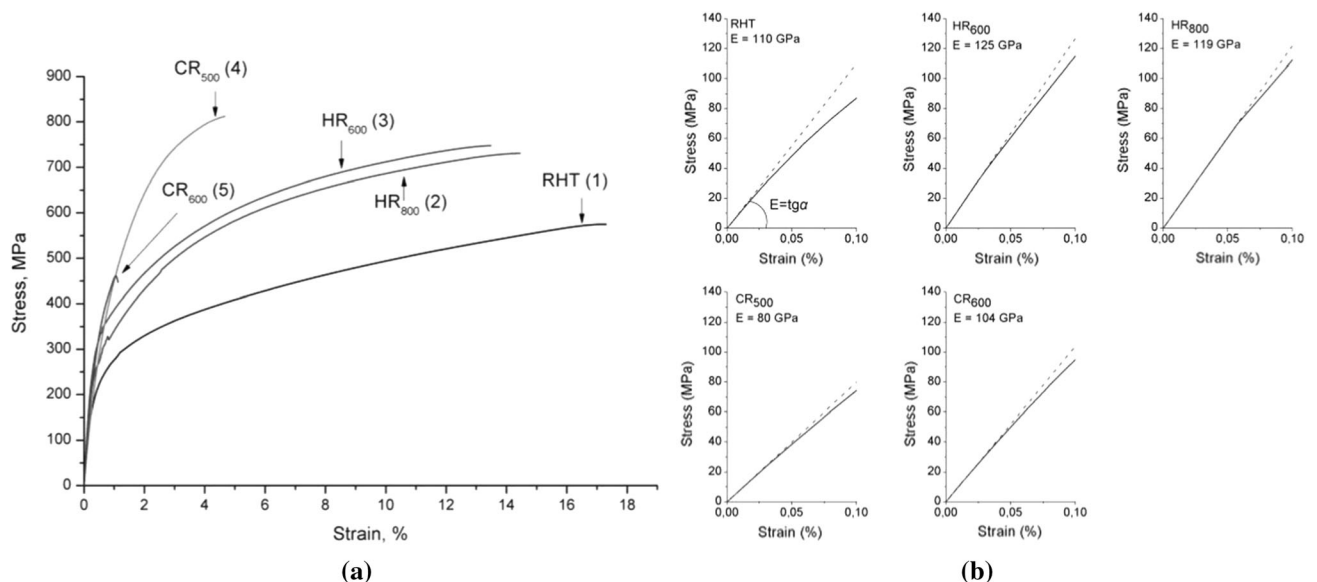


Fig. 4—Tensile stress–strain diagrams of the Fe-30Mn-5Si alloy after various treatments (a) and their enlarged fragments for calculating the Young’s modulus (b).

**Table IV. Mechanical Properties of the Fe-Mn-Si Alloy After Various Treatments**

Treatment	$E$ (GPa)	$\sigma_{0.2}$ (MPa)	$\delta$ (percent)	$\sigma_{UTS}$ (MPa)
RHT	110	190	17	585
HR <sub>600</sub>	125	320	14	755
HR <sub>800</sub>	119	260	15	725
CR <sub>500</sub>	80	390	5	865
CR <sub>600</sub>	104	380	1	500

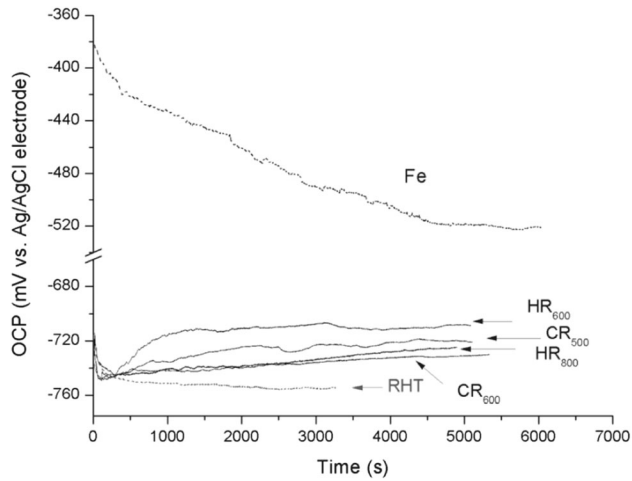


Fig. 5—OCP curves of the Fe-30Mn-5Si alloy after various treatments and Armco Fe immersed in Hanks' solution at 37 °C.

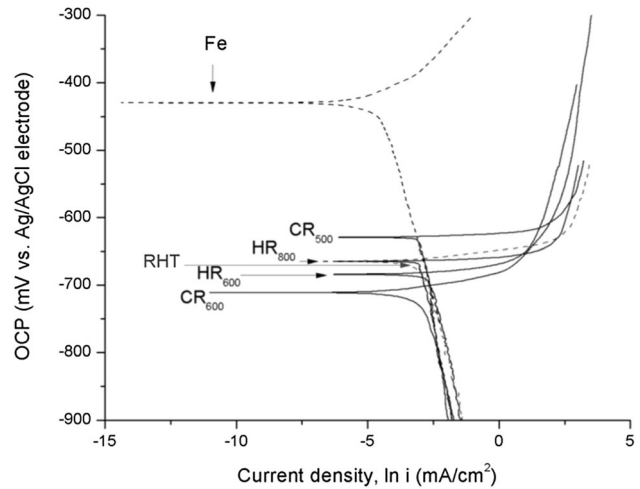


Fig. 6—Polarization diagrams of the Fe-30Mn-5Si alloy after various treatments and Armco Fe immersed in Hanks' solution at 37 °C.

active mode to the materials' dissolution; steady-state OCP values are observed in a certain period of immersion time. Two of the experimental findings are worth special mentioning: (1) the Fe-Mn-Si alloy exhibits a much shorter time to reach the steady OCP state (about several minutes) compared to Fe, which is important during an implant's performance parameters evaluation; (2) the Fe-Mn-Si alloy's steady-state OCP values after all TMT regimes are significantly more negative (by 200 to 230 mV) than that for Armco Fe, which indicates the remarkably higher electrochemical activity of the alloy.

Figure 6 shows the polarization diagrams of the studied materials immersed in Hanks' solution at 37 °C. In all cases, the corrosion proceeds with the cathodic control, which can be seen due to the significant slope of the cathodic (lower) branches of the polarization curves. All of the alloy's states feature the noticeable increase of the anodic dissolution rate compared to Armco Fe, which is evident from the sharp increase in current density even after a slight raise of the applied potential. The martensite  $\epsilon$ - and  $\alpha$ -phases act as the anodic regions, with the latter being present in trace amounts only after the RHT treatment and absent after TMT. The austenite  $\gamma$ -phase acts as the cathode; its volume fraction increases after TMT facilitates the cathodic process, *i.e.*, lowers its overvoltage, and consequently accelerates the anodic dissolution of the  $\epsilon$ -phase. The reason for the low dissolution rate of iron ( $\alpha$ -phase) is related to the high overvoltage of the

cathodic process caused by the low volume fraction of the carbide phase ( $\text{Fe}_3\text{C}$  or  $\text{Fe}_2\text{C}_6$ ), which acts as the cathodic regions (carbon content in Fe—0.014 wt pct [40]).

Table V summarizes the corrosion current density values of the Fe-Mn-Si alloy after various treatments and Armco Fe determined by the extrapolation of the polarization curves. It can be seen that all TMT regimes (except HR<sub>800</sub>) do not lead to a decrease in the corrosion rate compared to the RHT state. The lower corrosion rate of the HR<sub>800</sub> sample compared to HR<sub>600</sub> is presumably caused by (a) the lower number of defects on the recrystallized sample's surface, which contribute significantly to the surface energy and the corresponding reactivity value, (b) the deceleration of the anodic process due to a decrease in the fraction of the anodic regions represented by  $\epsilon$ -martensite, as shown by XRD results. It should be noted that in all structural states, the corrosion rate is several times higher than that of Armco Fe. The measured decrease in the corrosion rate of the Fe-Mn-Si alloy treated with HR<sub>800</sub>, as compared to the RHT and HR<sub>600</sub> states, can be considered as practically insignificant taking into account that this treatment regime ensures sufficiently low  $M_s$  temperature that is close to the human body temperature in combination with sufficient strength and plasticity. Therefore, this regime can be recommended along with HR<sub>600</sub> for bone implant biodegradable devices. For



**Table V. The Corrosion Rate of the Fe-30Mn-5Si Alloy After Various Treatments and Armco Fe Immersed in Hanks' Solution at 37 °C**

Treatment	Current density $i \cdot 10^5$ (A/cm <sup>2</sup> )	Corrosion rate $C_r$ (mm/year)
RHT	5.80 ± 0.3	0.69 ± 0.05
HR <sub>600</sub>	5.64 ± 0.36	0.62 ± 0.04
HR <sub>800</sub>	3.89 ± 0.33	0.47 ± 0.04
CR <sub>500</sub>	5.00 ± 0.5	0.60 ± 0.06
CR <sub>600</sub>	5.00 ± 0.5	0.60 ± 0.06
Fe Armco	0.87 ± 0.26	0.10 ± 0.03

further verification, corrosion fatigue studies will be valuable and are planned as the next step.

#### IV. CONCLUSIONS

The structure, phase composition, martensitic  $\gamma \leftrightarrow \varepsilon$  transformation temperatures, Young's modulus, mechanical properties, and electrochemical behavior of the Fe-30Mn-5Si (wt pct) biodegradable alloy after various thermomechanical treatment regimes were characterized by optical microscopy, EDX, XRD, DSC, tensile testing, open circuit potential, and polarization curves measurements in simulated biological solution mimicking the mineral content of bone tissue (Hanks' solution).

1. According to the XRD results, the TMT regimes including hot rolling (the true strain of  $e = 0.3$ , deformation temperature 600 or 800 °C) or cold rolling ( $e = 0.3$  with post-deformation annealing at 500 and 600 °C) lead to a decrease in the  $\varepsilon$ -martensite volume fraction at room temperature as compared to the reference heat treatment (homogenization annealing at 900 °C, 60 min followed by water quenching). The DSC measurements show a decrease in the starting temperature of the  $\gamma \rightarrow \varepsilon$  martensitic transformation  $M_s$ , which becomes close to the human body temperature.
2. The TMT preserves a low Young's modulus value of the studied alloy, in the range from 100 to 120 GPa, which is caused by the crystal lattice softening around the  $M_s$  temperature region exhibited due to an increase in the lattice defects concentration (dislocations, subboundaries, grain boundaries), leading to the lowering of the  $M_s$  towards the human body temperature.
3. The most significant increase in the yield stress  $\sigma_{0.2}$  (from 190 to 380–390 MPa) accompanied by the drastic drop of ductility compared to the reference state is observed after cold rolling with post-deformation annealing, which is caused by the highest concentration of lattice defects in the non-recrystallized state. Hot rolling at 600 and 800 °C results in less increase of the yield stress (up to 320 and 260 MPa, respectively) with a preserved plasticity level (14 to 15 pct) and high tensile strength, which is related to the development of the favorable

processes of dynamic polygonization and recrystallization in  $\gamma$ -phase.

4. The most practically appropriate TMT regime studied for the Fe-Mn-Si alloy is the hot rolling at 600 or 800 °C with subsequent water cooling, which provides the best combination of acceptable corrosion rate (0.5 to 0.6 mm/year) and  $M_s$  temperature closest to the human body temperature (about 40 °C), high mechanical strength, and appropriate ductility as compared to the reference treatment.

#### ACKNOWLEDGMENTS

The authors are thankful to Prof. Vladimir Brailovski from the Ecole de Technologie Superieure (Montreal) for his assistance in carrying out the DSC and mechanical tests. The work was carried out with the financial support of the Russian Science Foundation (Project # 19-79-10270), and RFBR (Project # 18-08-01193 A) in part of electrochemical characterization method optimization.

#### REFERENCES

1. J. Park and R.S. Lakes: *Biomaterials: An Introduction*, Springer, New York, 2007.
2. M. Saini, Y. Singh, P. Arora, V. Arora, and K. Jain: *World J. Clin. Cases*, 2015, vol. 3 (1), pp. 52–57.
3. N.S. Manam, W.S.W. Harun, D.N.A. Shri, S.A.C. Ghani, T. Kurniawan, M.H. Ismail, and M.H.I. Ibrahim: *J. Alloys Compd.*, 2017, vol. 701, pp. 698–715, <https://doi.org/10.1016/j.jallcom.2017.01.196>.
4. T. Narushima: *Metals for Biomedical Devices*, 2nd ed., M. Niinomi (ed.); Elsevier, 2019, pp. 495–521. <https://doi.org/10.1016/B978-0-08-102666-3.00019-5>.
5. F. Witte, A. Eliezer, and S. Cohen: *Adv. Mat. Res.*, 2010, vol. 95, pp. 3–7, <https://doi.org/10.4028/www.scientific.net/AMR.95.3>.
6. F. Witte and A. Eliezer: *Degradation of Implant Materials*, N. Eliaz (ed.), Springer Science + Business Media: New York 2012, pp. 93–109. [https://doi.org/10.1007/978-1-4614-3942-4\\_5](https://doi.org/10.1007/978-1-4614-3942-4_5).
7. H. Hermawan: *Biodegradable Metals - From Concept to Applications*, Springer, Berlin 2012. <https://doi.org/10.1007/978-3-642-31170-3>.
8. D. Vojtech, J. Kubasek, J. Capek, A. Michalcova, and I. Pospisilova: *Solid State Phenom.*, 2015, vol. 227, pp. 431–4, <https://doi.org/10.4028/www.scientific.net/SSP.227.431>.
9. M. Heiden, E. Walker, and L. Stanciu: *J. Biotechnol. Biomater.*, 2015, vol. 5, p. 1000178, <https://doi.org/10.4172/2155-952X.1000178>.



10. R. Drevet, Y. Zhukova, P. Malikova, S. Dubinskiy, A. Korotitskiy, Y. Pustov, and S. Prokoshkin: *Metall. Mater. Trans. A*, 2018, vol. 49, pp. 1006–13, <https://doi.org/10.1007/s11661-017-4458-2>.
11. Y. Su, I. Cockerill, Y. Wang, Y.-X. Qin, L. Chang, Y. Zheng, and D. Zhu: *Trends Biotechnol.*, 2019, vol. 37, pp. 428–41, <https://doi.org/10.1016/j.tibtech.2018.10.009>.
12. Y. Liu, Y. Zheng, X.-H. Chen, J.-A. Yang, H. Pan, D. Chen, L. Wang, J. Zhang, D. Zhu, S. Wu, K.W.K. Yeung, R.-C. Zeng, Y. Han, and S. Guan: *Adv. Funct. Mater.*, 2019, vol. 29, p. 1805402, <https://doi.org/10.1002/adfm.201805402>.
13. J. Venezuela and M.S. Dargusch: *Curr. Opin. Solid State Mater. Sci.*, 2020, vol. 24, art. no. 100822 <https://doi.org/10.1016/j.cossms.2020.100822>.
14. H. Kabir, K. Munir, C. Wen, and Y. Li: *Bioact. Mater.*, 2021, vol. 6, pp. 836–79, <https://doi.org/10.1016/j.bioactmat.2020.09.013>.
15. A. Sato, E. Chishima, K. Soma, and T. Mori: *Acta Metall.*, 1982, vol. 30, pp. 1177–83, [https://doi.org/10.1016/0001-6160\(82\)90011-6](https://doi.org/10.1016/0001-6160(82)90011-6).
16. T. Maki: *Shape Memory Materials*, K. Otsuka and C.M. Wayman (Eds.), Cambridge University Press, 1999, pp. 117–32.
17. V. Brailovski, S. Prokoshkin, P. Terriault, and F. Trochu: *Shape Memory Alloys: Fundamentals, Modeling and Applications; ETS*, ETS, Montreal, 2003.
18. A.A. Gulyaev: *J. Phys. IV*, 1995, vol. 5 (C8), pp. 469–74, <https://doi.org/10.1051/jp4:1995871>.
19. T.Y. Hsu and Z. Xu: *Mater. Sci. Eng. A*, 1999, vols. 273–275, pp. 494–7, [https://doi.org/10.1016/S0921-5093\(99\)00386-X](https://doi.org/10.1016/S0921-5093(99)00386-X).
20. A. Sato, Y. Yamaji, and T. Mori: *Acta Metall.*, 1986, vol. 34, pp. 287–94, [https://doi.org/10.1016/0001-6160\(86\)90199-9](https://doi.org/10.1016/0001-6160(86)90199-9).
21. E.Z. Vintaikin, A.A. Gulyaev, A.B. Oralbaev, N.A. Polyakova, and E.L. Svistunova: *Metallfizika*, 1991, vol. 13, pp. 43–51 (in Russian).
22. B. Liu, Y.F. Zheng, and L. Ruan: *Mater. Letters*, 2011, vol. 65, pp. 540–3, <https://doi.org/10.1016/j.matlet.2010.10.068>.
23. M. Fântăniariu, L.C. Trincă, C. Solcan, A. Trofin, S. Strungaru, E.V. Şindilar, G. Plăvan, and S. Stanciu: *Appl. Surf. Sci.*, 2015, vol. 352, pp. 129–39, <https://doi.org/10.1016/j.apsusc.2015.04.197>.
24. L.C. Trincă, L. Burtan, D. Mareci, B.M. Fernández-Pérez, I. Stoleriu, T. Stanciu, S. Stanciu, C. Solcan, J. Izquierdo, and R.M. Souto: *Mater. Sci. Eng. C*, 2021, vol. 118, art. no. 111436 <https://doi.org/10.1016/j.msec.2020.111436>.
25. H. Hermawan, A. Purnama, D. Dubé, J. Couet, and D. Mantovani: *Acta Biomater.*, 2010, vol. 6, pp. 1852–60, <https://doi.org/10.1016/j.actbio.2009.11.025>.
26. H. Hermawan, D. Dubé, and D. Mantovani: *J. Biomed. Mater. Res. A*, 2010, vol. 93A, pp. 1–11, <https://doi.org/10.1002/jbm.a.32224>.
27. M. Schinhammer, A.C. Hânzi, J.F. Löffler, and P.J. Uggowitzer: *Acta Biomater.*, 2010, vol. 6, pp. 1705–13, <https://doi.org/10.1016/j.actbio.2009.07.039>.
28. M. Schinhammer, C.M. Pecnik, F. Rechberger, A.C. Hânzi, J.F. Löffler, and P.J. Uggowitzer: *Acta Mater.*, 2012, vol. 60, pp. 2746–56, <https://doi.org/10.1016/j.actamat.2012.01.041>.
29. M. Rătoi, S. Stanciu, N. Cimpoesu, I. Cimpoesu, B. Constantin, and C. Paraschiv: *Adv. Mater. Res.*, 2013, vol. 814, pp. 110–14, <https://doi.org/10.4028/www.scientific.net/AMR.814.110>.
30. T. Kraus, F. Moszner, S. Fischerauer, M. Fiedler, E. Martinelli, J. Eichler, F. Witte, E. Willbold, M. Schinhammer, M. Meischel, P.J. Uggowitzer, J.F. Löffler, and A. Weinberg: *Acta Biomater.*, 2014, vol. 10, pp. 3346–53, <https://doi.org/10.1016/j.actbio.2014.04.007>.
31. H. Kitabata, R. Waksman, and B. Warnack: *Cardiovasc. Revasc. Med.*, 2014, vol. 15, pp. 109–16, <https://doi.org/10.1016/j.carrev.2014.01.011>.
32. N. Safaie, M. Khakbiza, S. Sheibani, and P. SotoudehBagha: *Procedia Mater. Sci.*, 2015, vol. 11, pp. 381–85, <https://doi.org/10.1016/j.mspro.2015.11.134>.
33. H. Li, Y. Zheng, and L. Qin: *Prog. Nat. Sci.*, 2014, vol. 24, pp. 414–22, <https://doi.org/10.1016/j.pnsc.2014.08.014>.
34. A. Francis, Y. Yang, S. Virtanen, and A.R. Boccaccini: *J. Mater. Sci.*, 2015, vol. 26, p. 138, <https://doi.org/10.1007/s10856-015-5473-8>.
35. J. Čapek, J. Kubásek, D. Vojtěch, E. Jablonská, J. Lipov, and T. Ruml: *Mater. Sci. Eng. C*, 2016, vol. 58, pp. 900–08, <https://doi.org/10.1016/j.msec.2015.09.049>.
36. Y.P. Feng, A. Blanquer, J. Fornell, H. Zhang, P. Solsona, M. DolorsBaró, S. Suriñach, E. Ibáñez, E. GarcíaLecina, X. Wei, R. Li, L. Barrios, E. Pellicer, and C. Nogués: *J. Sort. J. Mater. Chem. B.*, 2016, vol. 4, pp. 6402–12.
37. E. Mouzou, C. Paternoster, R. Tolouei, A. Purnama, P. Chevalier, D. Dubé, F. Prima, and D. Mantovani: *Mater. Sci. Eng. C*, 2016, vol. 61, pp. 564–73, <https://doi.org/10.1016/j.msec.2015.12.092>.
38. S. Stanciu, A. Ursanu, L.C. Trincă, T.A. Elena, S. Carmen, C. Munteanu, N. Cimpoesu, D. Acatrinei, E.V. Sindilar, T. Stanciu, M. Fântăniariu, and L. Topliceanu: *Environ. Eng. Manag. J.*, 2016, vol. 15, pp. 973–80.
39. M. Dehestani, K. Trumble, H. Wang, H. Wang, and L.A. Stanciu: *Mater. Sci. Eng. A*, 2017, vol. 703, pp. 214–26, <https://doi.org/10.1016/j.msea.2017.07.054>.
40. W. Lin, L. Qin, H. Qi, D. Zhang, G. Zhang, R. Gao, H. Qiu, Y. Xia, P. Cao, X. Wang, and W. Zheng: *Acta Biomater.*, 2017, vol. 54, pp. 454–68, <https://doi.org/10.1016/j.actbio.2017.03.020>.
41. Y. Li, H. Jahr, K. Lietaert, P. Pavanram, A. Yilmaz, L.I. Fockaert, M.A. Leeftang, B. Pouran, J. Gonzalez-Garcia, H. Weinans, J.M.C. Mol, J. Zhou, and A.A. Zadpoor: *Acta Biomater.*, 2018, vol. 77, pp. 380–93, <https://doi.org/10.1016/j.actbio.2018.07.011>.
42. M. CaligariConti, D. Aquilina, C. Paternoster, D. Vella, E. Sinagra, D. Mantovani, G. Cassar, P. SchembriWismayer, and J. Buhagiar: *Heliyon*, 2018, vol. 4, p. e00926, <https://doi.org/10.1016/j.heliyon.2018.e00926>.
43. P. Sharma and P.M. Pandey: *Mater. Sci. Eng. C*, 2019, vol. 99, pp. 838–52, <https://doi.org/10.1016/j.msec.2019.01.114>.
44. H.-S. Han, S. Loffredo, I. Jun, J. Edwards, Y.C. Kim, H.-K. Seok, F. Witte, D. Mantovani, and S. Glyn-Jones: *Mater. Today*, 2019, vol. 23, pp. 57–71, <https://doi.org/10.1016/j.mattod.2018.05.018>.
45. S. Mandal, R. Ummadi, M. Bose, V.K. Balla, and M. Roy: *Mater. Lett.*, 2019, vol. 237, pp. 323–27, <https://doi.org/10.1016/j.matlet.2018.11.117>.
46. S.M. Huang, E.A. Nauman, and L.A. Stanciu: *Mater. Sci. Eng. C*, 2019, vol. 99, pp. 1048–57, <https://doi.org/10.1016/j.msec.2019.02.055>.
47. Y.A. Pustov, Y.S. Zhukova, P.E. Malikova, S.D. Prokoshkin, and S.M. Dubinskiy: *Prot. Met. Phys. Chem. Surf.*, 2018, vol. 54, pp. 469–76, <https://doi.org/10.1134/S2070205118030139>.
48. J.H. Hanks and R.E. Wallace: *Proc. Soc. Exp. Biol. Med.*, 1949, vol. 71, pp. 196–200, <https://doi.org/10.3181/00379727-71-17131>.
49. R. Winston Revie (Ed.) *Uhlig's Corrosion Handbook*, 3rd Edition, John Wiley & Sons, Inc., 2011. <https://doi.org/10.1002/9780470872864>.
50. S.D. Prokoshkin, I.Y. Khmelevskaya, V. Brailovski, F. Trochu, S. Turenne, V.Y. Turilina, and K.E. Inaekyan: *J. Phys.*, 2003, vol. 112, pp. 789–93, <https://doi.org/10.1051/jp4:20031000>.
51. S.D. Prokoshkin, S. Turenne, I.Y. Khmelevskaya, V. Brailovski, and F. Trochu: *Can. Metall. Q.*, 2000, vol. 39, pp. 225–34, <https://doi.org/10.1179/cm.2000.39.2.225>.
52. V. Pushin: *Phys. Met. Metallogr.*, 2000, vol. 90, pp. S68–S95.
53. J.F. Wan, S.P. Chen, T.Y. Hsu, and Y.N. Huang: *Mater. Sci. Eng. A*, 2006, vols. 438–440, pp. 887–90, <https://doi.org/10.1016/j.msea.2006.02.152>.
54. K. Otsuka and C.M. Wayman: *Shape Memory Materials*, K. Otsuka and C.M. Wayman (Eds.), Cambridge University Press, 1999, pp. 1–26.

**Publisher's Note** Springer Nature remains neutral with regard to jurisdictional claims in published maps and institutional affiliations.